Violation of the Wiedemann-Franz law through reduction of thermal conductivity in gold thin films

S. J. Mason,[1,*] D. J. Wesenberg,[1,†] A. Hojem,[1,‡] M. Manno,[2] C. Leighton,[2] and B. L. Zink[1,§]

[1]*Department of Physics and Astronomy, University of Denver, 2112 East Wesley Avenue, Denver, Colorado 80208, USA*

[2]*Department of Chemical Engineering and Materials Science, University of Minnesota, 421 Washington Avenue Southeast, Minneapolis, Minnesota 55455, USA*

(Received 20 February 2020; revised manuscript received 29 April 2020; accepted 2 June 2020; published 24 June 2020)

We present measurements of in-plane thermal and electrical conductivity in thermally evaporated gold thin-film samples ranging in thickness from ≈20 to >300 nm, performed using a micromachined silicon-nitride membrane thermal isolation platform. In both ≈300-nm-thick films grown in a single Au deposition and a sample built up to >300 nm by many sequential depositions of thinner layers, we observe strong "violations" of the Wiedemann-Franz law that relates electrical and thermal conductivities. While electrical conductivity behaves essentially as expected, thermal conductivity first rises with growing total film thickness, and then surprisingly drops as the film becomes thicker. The sharp reduction of thermal conductivity decreases the Lorenz number L for ≈300-nm-thick samples to less than half the Sommerfeld value over the entire 78–300-K temperature range studied. Such violation near room temperature, in a metal film where electron transport should be well described by Fermi-liquid theory, is previously unreported, even in the presence of disorder introduced by grain boundaries and rough surfaces. This indicates an inelastic-scattering process that we argue, based on detailed characterization of grain size in these films, is likely driven by a combination of modified phonon density of states and structural anisotropy introduced from the strongly columnar grain structure in thicker films. This highly unusual reduction of thermal conductivity while maintaining high electrical conductivity is potentially promising for increasing thermoelectric performance of nanoscale systems.

DOI: 10.1103/PhysRevMaterials.4.065003

I. INTRODUCTION

The Wiedemann-Franz (WF) law, $k/\sigma = LT$, relating the ratio of thermal and electrical conductivities, k and σ, of charge carriers in a material to a constant Lorenz number L times temperature, T, is frequently used and highly trusted, as the underlying physics of electron transport in a Fermi liquid is typically robust. However, there are well-known "violations" of this relationship even in simple bulk metals for T near and below the Debye temperature, θ_D.[1] These occur when inelastic scattering of an electron from a state hotter than the average T into a colder than average state but with the same direction of transport tends to reduce k with little impact on σ [1]. Such events often occur between moderate-q phonons and conduction electrons, and are quenched by disorder in the material. Electron scattering from static disorder, such as occurs in the low T residual resistivity regime, is elastic and drives a return to WF-like behavior, albeit with L showing some dependence on material [2] and often deviating somewhat from the free-electron Sommerfeld value of $L_o = 2.44 \times 10^{-8}$ W Ω/K^2. Recently, more exotic violations of WF have been discussed in non-Fermi-liquid systems near quantum critical points at very low temperature [3,4], in one-dimensional (1D) or quasi-1D conductors [5–8], in unconventional superconductors and superconducting junctions (where σ diverges, but a similar relation exists between the Nernst and Hall coefficients) [9,10], or in correlated oxides such as VO_2 [11]. The WF law has also been validated for certain metals even at the scale of atomic junctions, however [12,13].

Current evidence therefore suggests that thin films of metals such as gold should be expected to obey the WF law, and indeed we have recently shown that a ≈100-nm-thick gold film shows WF behavior from 77 to 325 K with a value of $L = 2.1 \times 10^{-8}$ W Ω/K^2 reduced only slightly from bulk gold [14]. Earlier work showed that much thinner 18-nm films also matched expectations from the WF law [15]. We have also shown excellent agreement with the WF law in a Ni-Fe film, where disorder scattering from the random alloy dominates, and that only slight reductions in L occur near room temperature for Cu, Co, Ni, Al, and Mo films in the thickness range near 100–200 nm [16–18]. We also identified positive deviations from the WF law as T drops, which suggests a possible phonon contribution to k in Cu [16]. Phonon contributions to thermal conductivity in metals and semiconductors are in fact being investigated with new theoretical and computational tools [19–22], and can be

*Present address: Broadcom, Ltd., Fort Collins, Colorado 80525, USA.

†Present address: Lam Research, Portland, Oregon 97062, USA.

‡Present address: Department of Physics, University of California, San Diego, La Jolla, California 92093, USA.

§Corresponding author: barry.zink@du.edu

[1]We use quotation marks around violations to indicate that, since the WF law is not a robust physical law, deviations simply indicate the presence of other physical phenomena, as discussed here in detail.

important even in bulk. Nevertheless, the best current picture seems to suggest that, in thin films of gold, phonons contribute on the order of 10% or less of the total thermal conductivity [19], though this estimate will depend on the thickness, grain size, and other details. Note that in previous work we have neither extensively studied the thickness dependence of L nor investigated gold films thicker than $\approx$100 nm.

Reliable measurements of thermal conductivity on nanostructures or metal films with thickness of tens to hundreds of nanometers are typically difficult due to the presence of a large background thermal conductance from the supporting substrate. Nevertheless, several reports have examined k in these metallic systems, including studies suggesting that gold films of thickness $<$100 nm violate WF with values of L *exceeding* the Sommerfeld value somewhat in the regime near room temperature [23–25], with L growing even larger as the temperature is reduced toward 3 K. Other studies of nanoporous Au foils showed reasonable agreement with the WF law with a somewhat enhanced value of L [26]. Free-standing tungsten nanobridges have also been shown under some conditions to exhibit larger k than predicted by the WF law [27]. Kojda *et al.* showed that a single-crystal Ag nanowire, proven via *in situ* TEM characterization to be highly crystalline, showed a temperature-dependent Lorenz number that very closely matched the expectation of the WF law, taking into account the simple model of electron-phonon (e-ph) scattering developed for bulk systems [28]. This contrasts with Cheng *et al.*, who reported large values of L in polycrystalline Ag nanowires [29]. All of these positive deviations could be explained by additional thermal conductivity via phonons in systems with strongly reduced electrical conductivity, through disorder or boundary scattering.

Measurements of Au and Pt nanowires are among the few reports of *reduced* L in nanostructures, though usually these show that both σ and k (and $d\rho/dT$) are strongly modified. These include measurements of free-standing Pt nanowires [30,31] and, more recently, ultrathin Au nanowires in experiments where the wires were supported by a bulk substrate [32]. Lee *et al.* also reported that metallic vanadium dioxide in the region near the metal-insulator transition has strongly reduced k [11], which they related to VO_2's strongly correlated nature and "bad metal" behavior, where normal quasiparticle expectations do not apply. Other earlier studies of k in metal thin films conducted via a range of techniques (usually with the presence of a bulk substrate) report reduced k compared to bulk values, as expected, but usually with some reduction of σ, and approximate agreement with the WF law, though the validity of the WF law for thin polycrystalline metal films has never been clearly established [33–35].

Significantly, the balance between σ and the electronic thermal conductivity k_e is almost always an important limitation on the thermoelectric efficiency of a material used to convert waste heat to electricity via the Seebeck effect, or to cool objects via the Peltier effect [36–42]. As a result, a means to lower k while keeping σ high is of tremendous interest to the thermoelectric materials community. Note that the known violations of the WF law in thin metal films are all toward the unhelpful direction of improved k and decreased σ. Here, we present measurements of thin-film gold samples that achieve the "desired" violation of the WF law, i.e., lowering k while maintaining approximately constant σ. A similar reduction of k in a one-component metal film with larger intrinsic Seebeck coefficient could produce simple thermoelectric elements with favorable power factor and double the thermodynamic efficiency.

Specifically, in this paper we report large violations of the Wiedemann-Franz law in evaporated gold films in the temperature regime near room temperature. In contrast to reports in most other metallic nanostructures, these deviations correspond to *reductions* from L_o, driven by reduced thermal conductivity. After introducing our measurement technique, which, due to the geometry of the thermal isolation platform, exclusively measures in-plane transport, we present detailed structural characterization of the films before continuing to results showing a dramatically reduced Lorenz ratio for a range of different Au films. We conclude with comparisons to simple theoretical predictions, and with a suggestion of a potential mechanism for the thermal conductivity reduction based on modification of the phonon density of states in these nanograined polycrystalline Au thin films.

II. EXPERIMENT

Our approach to measurements of k in films with nanoscale thickness focuses on removing macroscopic heat sinks by supporting the sample, heaters, and thermometers, and all measurement leads, on a free-standing silicon nitride membrane. This allows realization of the simple thermal model shown in Fig. 1(a), where two heat capacities are connected to the heat sink of a bulk substrate through thermal conductances, K_L, formed only from Si-N supports and thin-film leads. Before the addition of a sample, the two are linked by a Si-N bridge with thermal conductance K_B. Subsequent deposition of Au thin films through a shadow mask adds additional thermal conductance K_{Au}. The use of this model assumes that any cross-plane thermal interface resistance is small compared to the in-plane thermal resistances. This is a very good assumption, since the large interfacial areas [between at least the Au film and the large platinum electrical contacts visible in Fig. 1(b)] and typical Au/Pt interfacial conductance of 0.2 GW m^{-2} K^{-1} or greater [43] make any out-of-plane thermal boundary conductance at least four orders of magnitude larger than any in-plane thermal conductance in the suspended structure.

An example thermal isolation platform is shown in a scanning electron micrograph in Fig. 1(b), where the two Si-N islands, each with separately patterned resistive thermometers and heaters, are visible along with the supporting legs and sample bridge. The area where thin-film samples are deposited is shown schematically, and the pattern of heating in response to constant power added to the left island heater is shown with false color. Note that the sample area bridging the islands is $\approx$2 mm long, while the films studied are $<$400 nm thick. This extreme aspect ratio ensures that our measurements exclusively probe in-plane k and σ.

The gold films we study here are grown via thermal evaporation in high vacuum at rates $\approx$0.1 nm/s from source material with 99.999% purity after reaching base pressures of 10^{-6} Torr or better. In addition to the thermal isolation platforms, we also grow films on Si-N coated bulk Si substrates (the same

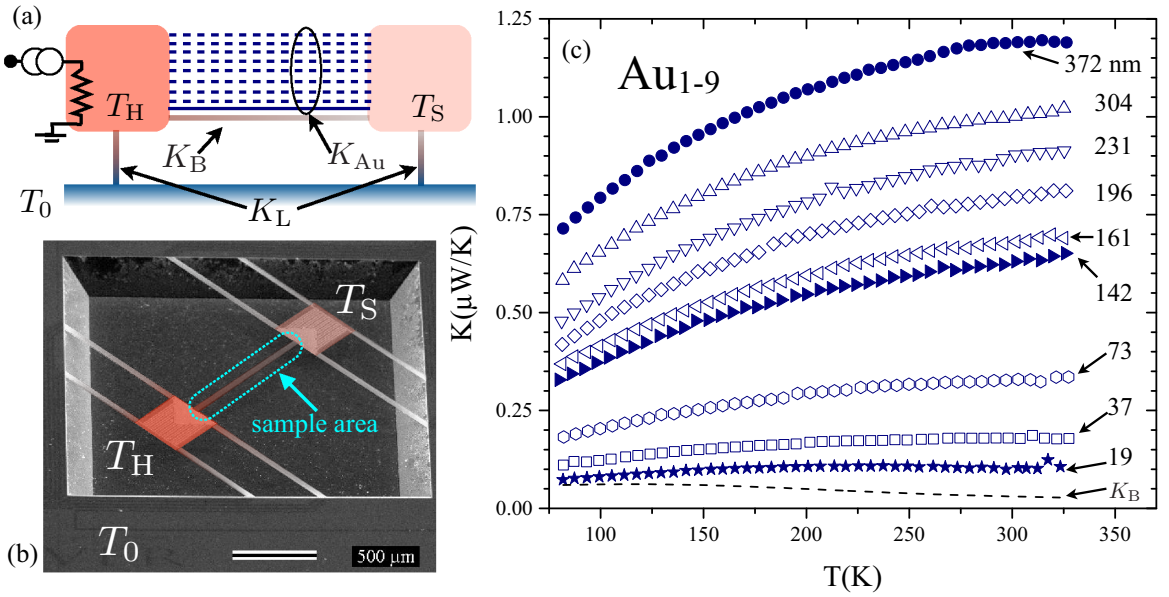

FIG. 1. (a) Thermal model of the suspended Si-N structure and sample films used to determine the sample thermal conductance, K. Dashed lines indicate the sequential deposition of Au films used to produce samples Au_{1-9}. The same thermal model with a single sample K represents samples Au_0 and Cr/Au. (b) False-color tilted scanning electron micrograph of the suspended Si-N thermal isolation platform. The two thermal stages at T_H and T_S and the bridging sample platform are indicated. (c) K vs T for the thermal isolation platform used for nine sequential Au depositions and measurements. The dashed line is the Si-N background, K_B, and dark blue symbols indicate measurements after deposition of Au films. The numbers at right give the total thickness of the Au film after each sequential deposition.

as used for nanofabrication of the thermal isolation platforms) for complementary structural characterization and thickness measurements via atomic force microscope profilometry. We grew three types of Au film for this paper: a first deposited on the same thermal isolation platform in nine sequential steps, with measurements of the platform after each deposition (labeled Au_{1-9} in the figures that follow, where single-number subscripts indicate a single layer of this film); a second labeled Au_0, which we grew to a similar total thickness but in a single deposition; and finally another ≈300-nm-thick single-shot film grown after deposition of a 10-nm Cr adhesion layer as is typical for growth of Au on oxidized or nitridized substrates, which we label Cr/Au.

Au films were characterized structurally using x-ray diffraction (XRD), atomic force microscopy (AFM), and scanning electron microscopy (SEM). XRD scans were performed using a Bruker D8 Discover x-ray diffractometer equipped with a Co source, an incident beam graphite monochromator, and a two-dimensional x-ray detector. For each sample, three two-dimensional datasets were collected, and then integrated and merged to a single one-dimensional XRD pattern with scattering angles converted to an equivalent Cu source x-ray wavelength for ease of analysis. AFM measurements used two different instruments depending on the characterization performed. Measurements that determined film thickness used an Asylum MFP3D microscope in contact mode, while lateral grain size and surface roughness measurements were performed using a Nanosurf NaioAFM operating in contact mode. Finally, secondary electron imaging (SEI) and backscattered electron imaging (BEI) SEM measurements were collected using a JEOL JSM-6010PLUS/LA operating at 20 kV.

We measure the thermal conductance of the bridge (including any additional sample) after mounting the thermal isolation platform chip on a radiation shielded sample mount in a sample-in-vacuum cryostat. We measure the temperatures T_H and T_S in response to power P added to the island heater after the very short wait required to establish thermal equilibrium in the entirely thin film heater. The simple thermal model of Fig. 1(a) relates K_B and K_L to P, such that

$$T_H = T_o + \left[\frac{(K_L + K_B)}{(2K_B + K_L)K_L}\right]P, \quad (1)$$

$$T_S = T_o + \left[\frac{K_B}{(2K_B + K_L)K_L}\right]P, \quad (2)$$

where we have assumed the small ΔT limit. To increase measurement accuracy we typically measure T_H and T_S for a range of applied P and make linear fits to these values plotted vs P. The slopes of these fits allow extraction of K_B and K_L. We determine the contribution from the sample by first measuring K_B with no film added, then subtracting this background value from the measured thermal conductance after adding a sample film. Figure 1(c) shows measured K_B (dashed line) and total $K = K_B + K_{Au}$ (blue symbols) for the platform used to measure Au_{1-9}. At right we indicate the total thickness of the Au film after each sequential deposition. K_B is in line with our previous measurements for similar platforms, with values <100 nW/K. Addition of thick Au films increases the total K by more than a factor of 10. We described details of the microfabrication and further details of use of these platforms elsewhere [14,16,18].

One important advantage to this technique is that, in addition to measuring thermal conductance K, we also use four

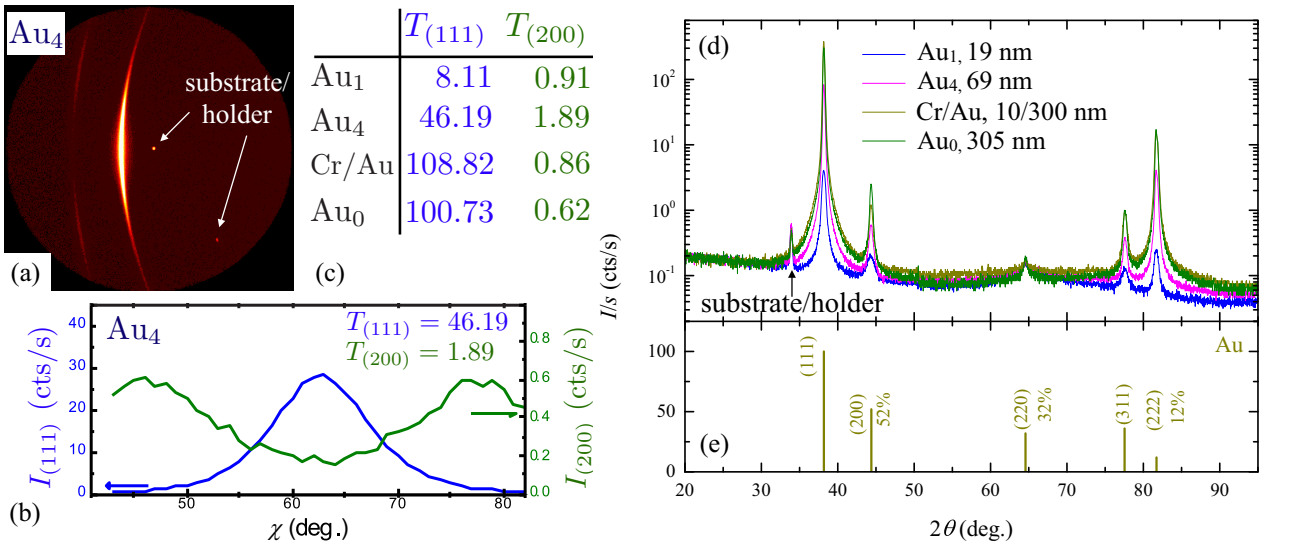

	$T_{(111)}$	$T_{(200)}$
Au_1	8.11	0.91
Au_4	46.19	1.89
Cr/Au	108.82	0.86
Au_0	100.73	0.62

FIG. 2. (a) XRD area detector image taken for film Au_4, centered at $2\theta \sim 34°$, with an angular width $\approx 30°$. The intensity in the two rings is clearly not uniform, visually indicating texturing of the sample. (b) An example plot of XRD intensity I vs angle χ for Au_4, showing nonuniformity for the two bright rings. (c) Comparison of normalized peak height $T_{(111)}$ and $T_{(200)}$ for four films indicating highly (111) textured films. (d) X-ray intensity I/s (logarithmic scale) vs 2θ for four Au films, Au_1, Au_4, Cr/Au, and Au_0. (e) Expected relative intensity for a random Au polycrystalline material, plotted as percentage of expected intensity. Note the measured (111) and (222) peaks are dramatically stronger than the reflections from other planes, one indication of strong texturing in the (111) direction.

additional leads, two of which are visible in Fig. 1(b) as large triangular pads at each end of the indicated sample area, to measure the electrical resistance R for the exact same film at each step of the measurement. Electrical resistivity ρ and thermal conductivity k are then determined from the sample geometry. To examine the Lorenz number and study violations of the WF law, we have

$$L = \frac{k}{\sigma T} = \frac{K_{\text{film}} R_{\text{film}}}{T}. \tag{3}$$

This means that the geometry of the sample, often the dominant source of systematic error in transport measurements on thin-film samples, does not enter in the determination of L. As discussed further in Sec. IV, for films with very low thermal conductance, some uncertainty arises due to small changes of the Si-N background thermal conductance due to surface scattering effects [14]. But, as we show in Fig. 1(c), for the Au_{1-9} film, the contributions to total K for all but the first film are much larger than the ≈10-nW/K changes possible from that effect. Even for films near 40-nm thickness, the thermal conductance of the Au is more than double the contribution from the 500-nm-thick Si-N bridge.

III. RESULTS

A. Structural characterization

Before detailing the quite dramatic in-plane heat and charge transport properties of these films, we first present structural characterization that shows that in all cases these are fairly typical polycrystalline films with microstructure well in line with expectations for evaporated films. Figure 2(a) shows an example XRD area detector image, representative of data taken for four of the Au layers, Au_1 (the first in the sequence of nine evaporations), Au_4 (the fourth in that series), Au_0, and Cr/Au. This image shows diffraction from Au_4 centered at $2\theta \sim 34°$ with a total angular range $19° < 2\theta < 59°$. Reflections from two sets of planes are visible here, and both show nonuniform intensity around each arc, indicating texturing of the film. We quantify this variation in intensity for the two rings in Fig. 2(b), which plots integrated intensity I as a function of the angular position on the ring, χ. Here the blue trace shows I for the (111) ring on the left y axis, and the green trace shows I for the (200) ring on the right y axis. The right axis has a ≈50× smaller range, meaning that the intensity of the (111) peak is much more sharply peaked. We compare the normalized peak height for all four Au layers examined in Fig. 2(c), where

$$T_{(\text{hkl})} = \frac{(I_{\max} - I_{\min})}{I_{\min}}, \tag{4}$$

with $I_{\max}$ ($I_{\min}$) the peak (baseline) intensity for each ring. This shows more strongly peaked distributions for (111) than for (200) across all films, with a trend toward even sharper peaking with increasing thickness of the Au layer.

Figure 2(d) shows x-ray intensity I vs 2θ x-ray-diffraction patterns, determined by integrating area images such as Fig. 2(a) for three different ranges of 2θ for the four Au layers. The measured thickness of each layer is given in the caption of the top panel, and the expected Bragg diffraction peak positions and relative intensity for a random Au polycrystal are indicated in the bottom panel. With the exception of a narrow peak near $2\theta = 34°$ that the area scan of Fig. 2(a) indicates is a single diffraction spot that results from the substrate or sample holder, all the measured peaks are indexed to expected FCC Au diffraction. For the Cr/Au sample, the 10-nm-thick Cr is most likely too thin to resolve, and the overlap of the fcc Au and bcc Cr peaks would prevent separation of these. Note also that the (111) and (222) peaks are very strong

TABLE I. Thickness, grain size, and film roughness determined from XRD and AFM. Thickness determined from AFM contact mode profilometry of Au_1 and Au_4 has an uncertainty of 2 nm or less, and the thicker Au_0 film has a somewhat higher 8-nm uncertainty. In-plane and out-of-plane grain sizes are estimated from XRD peak widths as described in the text.

Sample	t_{film} (nm)	$d_{g,OP}$ (nm)	$d_{g,IP}$ (nm)	$d_{g,IP,AFM}$ (nm)	σ_{AFM}
Au_1	19	23	11	40 ± 5	1.36
Au_4	69	71	28	48 ± 5	1.36
Cr/Au	10/300	74	30	82 ± 7	3.43
Au_0	305	>100	37	61 ± 6	3.14

relative to the other (hkl) planes, indicating that all films studied here are not simply random polycrystals but show significant out-of-plane texturing in the (111) direction. The width of the peaks shown here is also large compared to the instrumental broadening, so that average crystallite size can be estimated using Scherrer's formula, with the assumption of zero microstrain. Furthermore, the textured nature of the films allows approximate estimation of the in-plane and out-of-plane grain sizes, since the (111) and (222) peaks are typically parallel to the substrate, while the (200) and (311) planes are on average more tilted in the in-plane direction. The resulting estimates for in-plane grain size, $d_{g,IP}$, and out-of-plane grain size, $d_{g,OP}$, appear in Table I. Here we see in general that the estimated in-plane grain size remains relatively constant with thickness in the range 11–37 nm, while $d_{g,OP} \approx t$, indicating the presence of columnar grains. Such a grain structure is common for a fairly wide range of surface, grain, and bulk free energies, and very reasonable for these films evaporated at relatively low rates at low temperature onto amorphous substrates [44]. Both thinner layers, Au_1 and Au_4, likely consist of a single layer of these grains, while thicker films could be several grains thick.

Figure 3 shows 1×1 μm atomic force micrographs of the top surface of the same four Au films examined with XRD in Fig. 2. These images confirm the picture from XRD, with relatively small, roughly circular grain patterns. Both the average grain size of this top surface, $d_{g,IP,AFM}$, and the rms roughness also appear in Table I. Here a trend toward slightly larger in-plane grains for the thicker films is apparent, which suggest a slight conical shape to the columnar grains, as is also common for evaporated metallic films [44]. The AFM image of film Au_1 also shows several voids (the black areas) where individual grains or small groups of grains are apparently missing. We believe this is the result of damage to this very thin film from handling after growth (including measurements of residual resistivity at ≈4 K). We cannot confirm or exclude that such voids formed in the sample used to measure k and σ, which can introduce systematic errors into the calculation of these quantities from K and R. However, we emphasize that our measurements made on exactly the same samples for K and R yield correct values of L even if the sample geometry is difficult to determine due to formation of pores or voids.

Finally, we confirm that the grains are fully coalesced using scanning electron microscopy of the same samples with two imaging techniques. We show the results for the Au_1, Au_4, and Cr/Au and samples in Fig. 4. Here the left micrographs use the typical SEI mode, and the right micrographs use BEC. Backscattered electrons are more strongly affected by the total Z number of the sample atoms, and contrast in such images indicates changes in atomic composition. Here the SEI images show similar morphology to AFM for all three films, including the dark regions in Au_1. The BEC image for this film shows strong contrast in these regions, caused by the large difference in Z for the Au film and underlying Si-N and Si substrate. This confirms the voids for Au_1 (which would not affect our L measurements even if present for the Au_1 film on the suspended platform at the time of its k and σ measurements, as discussed above), and also shows that such voids do not exist in the thicker films, where very little contrast is visible in the BEC mode. These images confirm the Au films studied here are continuous, highly textured polycrystalline films, very much in line with expectations for thermally evaporated films grown on an amorphous substrate.

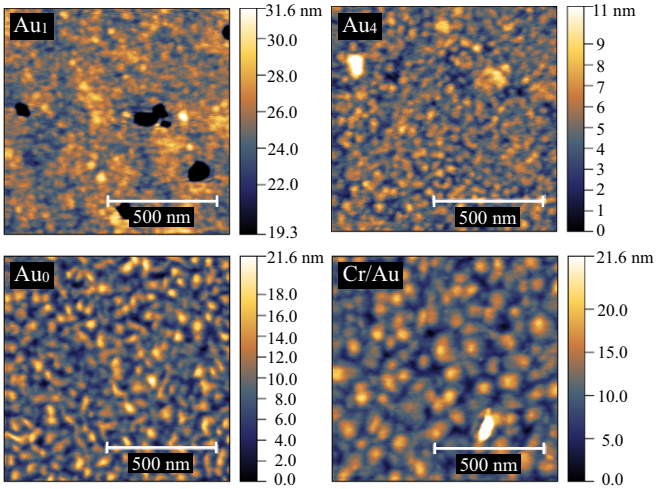

FIG. 3. Contact mode atomic force micrographs of four of the evaporated Au films show small, roughly circular grains that grow and coalesce as the total film thickness grows. The black areas visible in the scan of Au_1 are voids most likely caused by damage to this thin, relatively fragile Au film (with no adhesion layer) that occurred during handling of this substrate. These areas were excluded from numerical analysis for grain size and roughness. Note also that the color scale begins at 19.3 nm for only that sample. The height variations in the image are ≈20 nm, in line with the measured thickness of this film.

B. Transport measurements and WF violation

Figure 5 reports the T dependence of k, ρ, and L/L_0 for Au_{1-9}, Au_0, and Cr/Au films. We first show k vs T in Fig. 5(a). As expected, k for these films ranging from ≈20 to ≈ 380 nm thick are well below accepted values for bulk Au at all T. Bulk values are not shown, but lie near 300 W/mK through this entire T range [45]. Note that in Fig. 1(c) for films Au_{1-9}, though the total thermal conductance K always grows when material is added, the thermal conductivity actually drops at higher T when total t grows greater than 150 nm, indicating a very different scaling than expected. This dependence on t is shown explicitly at two

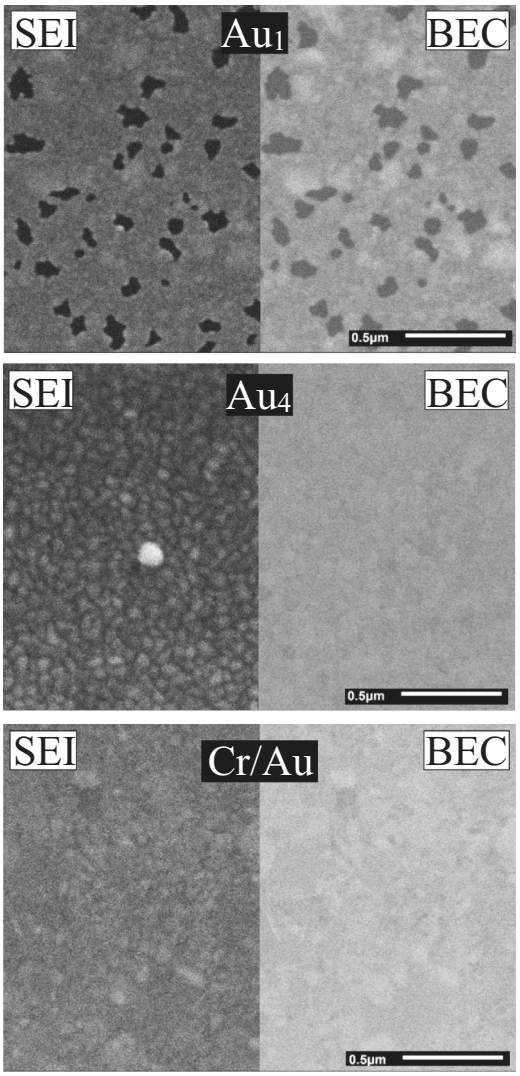

FIG. 4. Scanning electron micrographs of Au_1, Au_4, and Cr/Au and films (Au_0 was also analyzed, but not shown here), in the standard secondary electron imaging (SEI) and backscattered electron collection (BEC) modes. The lack of contrast in the BEC scans, which are more dependent on atomic composition of the sample, indicate that all but the thinnest Au thin films are formed from fully coalesced grains. The voids in Au_1 clearly correlate with features in both SEI and BEC images.

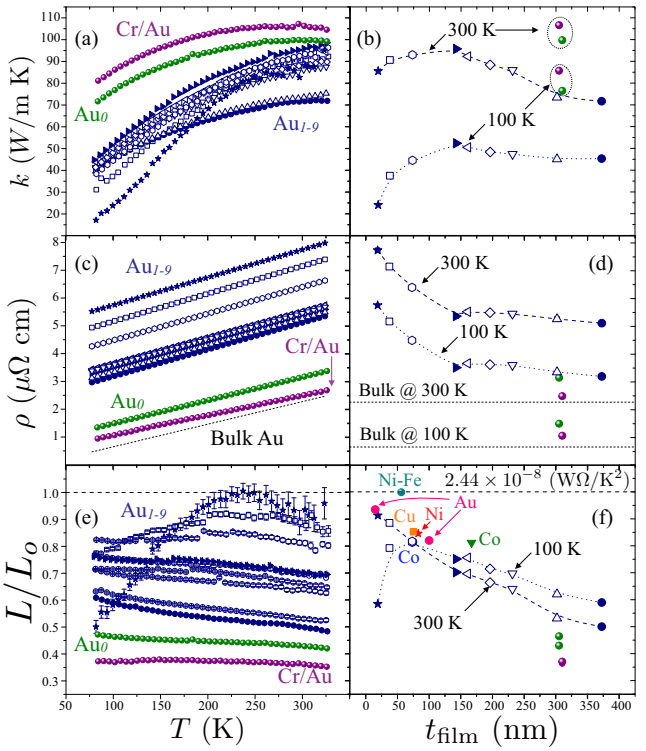

FIG. 5. k, $\rho = 1/\sigma$, and L for evaporated gold films. Panels (a), (c), and (e) show these quantities as a function of T and (b), (d), and (f) show the same data at select T as a function of film thickness, t_{film}. Surprisingly, the Au films show a strong trend toward suppression of L with increasing thickness. Note that especially for the single-layer films ρ approaches bulk values (dashed line), and the drop in L to $<0.4L_0$ is driven almost entirely by reduction in k_e. Also shown in (f) are $T = 300$ K L values for other metal films of similar thickness measured with the same techniques [16]. This includes two previous measurements of 15- and 100-nm-thick Au films (pink circles) [14].

temperatures, 300 and 100 K, in Fig. 5(b), where the change in the overall trend of k vs t at 150 nm is distinct. This clearly shows the dependence on sample thickness is more complicated than expected. Classical finite-size effects would suggest that $1/k$ scales as $1/t$, or that $k \propto t$, where t is film thickness. Note that even the thickest films, where t is large compared to all relevant length scales for the electrons, are still well below bulk values for Au. However, the 300-K values for films Cr/Au and Au_0 approximately align with t-linear behavior extrapolated from the thinnest films in the Au_{1-9} series.

Similar plots for ρ vs T and t, measured for the same Au films, appear in Figs. 5(c) and 5(d). Here we see much more typical behavior for thin film Au, with the expected high T approximate linear behavior for all films, with the highest ρ observed for the thinnest films, and values for very thick films that approach but do not achieve bulklike ρ, with bulk ρ shown as the dashed line [46]. Behavior with t is closer to expectations from classical finite-size effects, though thicker films in the Au_{1-9} series do have somewhat worse conductivity than expected. Again, a discontinuity in the overall trend with t occurs at 150 nm. It is possible that this change in transport, with ρ remaining higher than the classical finite-size $1/t$ extrapolation would suggest and k remaining lower, could be caused by the formation of a second layer of columnar grains in the thicker films. The nearly bulklike ρ for the thick single-layer films while their k stays more than 1/3 lower than bulk is a striking initial piece of evidence of the violation of the WF law.

These violations are most clearly shown by plotting the measured Lorenz number, which Eq. (3) shows is independent of sample geometry. Figures 5(e) and 5(f) show this value, scaled by the free-electron Sommerfeld value, vs T and t. The thinnest film, Au_1, is near expectations for the WF law at the highest T, but rapidly drops, reflecting the reduction of k, as T drops. Thicker layers have reduced L at all T, with the most dramatic reduction evident in the Cr/Au film, which has L nearly independent of T and reduced to less than

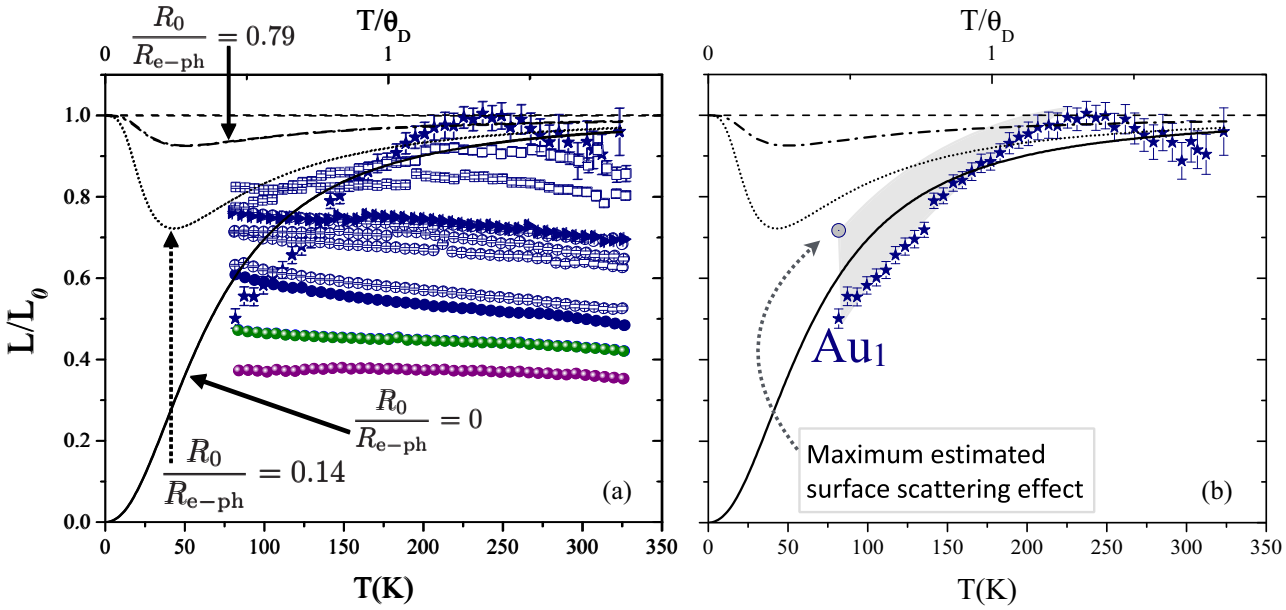

FIG. 6. Comparison of measured $L(T)$, scaled here using the Sommerfeld value L_0, to the theoretical expression of Eq. (5). (a) $L(T)/L_0$ vs T for all Au films compared to three theory values: a calculation including no impurity scattering $R_0/R_{e-ph} = 0$, one with $R_0/R_{e-ph} = 0.14$ calculated from measured ρ_0 for Au_0, and $R_0/R_{e-ph} = 0.79$ calculated from measured ρ_0 for Au_1. Thicker Au films show strong suppression of $L(T)/L_0$ at all T. (b) Plot of only Au_1, with the gray circle and filled area indicating the maximum possible uncertainty due to changes in surface scattering in the Si-N as described in the main text. We conclude that Au_1 roughly agrees with $L(T)$ theory for no impurity scattering, indicating possible increase of electron-phonon scattering in this film.

40% of the simple free-electron expectation. On the L/L_o vs t plot shown in Fig. 5(f), we compare the Au films to other measurements our group made on other metallic films, as well as two previous measurements of thinner Au films. A Ni-Fe alloy film showed the best agreement with the WF law, as expected from the dominant elastic impurity scattering in such an alloy, while other pure elemental evaporated films show only slight reductions at room T [16]. Our previous $t = 15$- and 100-nm Au films (pink circles) are very much in line with the trend shown for this group of Au films, where suppression of L grows largest at large t. Again we clarify that these dramatic reductions in L/L_0 are driven by k, and that these values are all measured for the same samples for both k and σ, so no error is introduced by uncertainty in sample geometry.

IV. DISCUSSION

We conclude with a consideration of the possible physics driving the reduced k in these Au films, though it is clear that further study and theoretical consideration will be required for a rigorous understanding of this effect. The main results from our paper are clear from Figs. 5(e) and 5(f), which show the dramatic reduction in L for a wide range of T and film thickness. This sort of reduction of L suggests strong inelastic small q phonon scattering of the electrons involved in thermal conduction. We begin a consideration of possible physical mechanisms for this reduction by comparison with the simple theory for $L(T)$ developed for bulk metals. The theoretical expression for the Lorenz ratio, $L_{Th}(T)/L_0$, as a function of temperature that takes into account electron-phonon and impurity scattering, is given by [35,47]

$$\frac{L_{Th}(T)}{L_0} = \frac{\frac{R_0}{R_{e-ph}} + \left(\frac{T}{\theta_D}\right)^5 J_5\left(\frac{\theta_D}{T}\right)}{\frac{R_0}{R_{e-ph}} + \left(\frac{T}{\theta_D}\right)^5 J_5\left(\frac{\theta_D}{T}\right)\left[1 + \frac{3}{\pi^2}\left(\frac{k_F}{q_D}\right)^2\left(\frac{\theta_D}{T}\right)^2 - \frac{1}{2\pi^2}\frac{J_7\left(\frac{\theta_D}{T}\right)}{J_5\left(\frac{\theta_D}{T}\right)}\right]}. \quad (5)$$

Here k_F is the Fermi wave vector; θ_D and q_D are the Debye temperature and wave vector, respectively; and

$$J_n\left(\frac{\theta_D}{T}\right) = \int_0^{\theta_D/T} \frac{x^n e^x}{(e^x - 1)^2} dx, \quad (6)$$

with $n = 5$ or 7. The ratio R_0/R_{e-ph} quantifies the level of impurity scattering, where R_0 is the residual resistance and R_{e-ph} is the contribution from electron-phonon scattering. Though this expression involves a number of assumptions including spherical Fermi surfaces, equilibrium phonon distributions, and normal (N) scattering processes (discarding umklapp processes), for electron-phonon scattering, it has been used to analyze noble-metal nanostructures, which showed excellent agreement with the theory for silver nanowires with confirmed high degree of crystallinity via TEM, for example [28]. This is due in part to the nearly spherical Fermi surface for Au and Ag.

We compare our results for Au to this theory in Fig. 6. Here we plot $L(T)/L_0$ vs T, with T/θ_D also shown on the top axis, where $\theta_D = 165$ K is the high T value for gold's Debye temperature. Figure 6(a) shows the entire range of films, compared to the theoretical value calculated for three different

impurity scattering amounts: $R_0/R_{e-ph} = 0$, the case of zero impurity scattering, and $R_0/R_{e-ph} = 0.79$ and 0.14. The latter two are calculated using the measured residual resistivity (taken from 5-K values of ρ) for Au_1 and Au_0, respectively. As in earlier work [16,28], we determine $R_0/R_{e-ph} = \rho_0/\rho_{e-ph}$ with the expression $\rho_{e-ph} = (d\rho/dT)T$, which is a reasonable assumption for the Au films at these T where $d\rho/dT$ is predominantly linear and nearly equal to that for bulk values [28,35]. Here we see that the thinnest film (the $t = 19$ nm first layer in the sequential series labeled Au_1 shown with blue stars) has the strongest T dependence, and roughly matches the prediction of the $L(T)$ theory when impurity scattering is ignored. As the film grows thicker, the T dependence becomes weaker, while the overall suppression of L grows. This indicates that the balance of horizontal and vertical electron-phonon scattering, as discussed further below and shown schematically in Fig. 8(a), changes as the Au films grow thicker.

The strong T dependence of the thinnest films is striking. In our previous work using suspended Si-N platforms to study thin-film thermal conductivity, we have observed changes in the Si-N background thermal conductance driven by surface scattering of long-wavelength phonons in the Si-N by the addition of a sample film [14]. This change in the background can cause apparent reduction in k for thin-film samples with a small additional thermal conductance K_{Au} [16]. Before continuing discussion of the thinnest Au films we must rule out Si-N phonon surface scattering as a cause of the drop in k and L at lower T. The largest total drop in K_B we have observed is a shift of 10 nW/K. In Fig. 6(b), we plot only $L(T)/L_0$ for Au_1. The labeled gray circle is the result if we assume that K_{Au} has the largest possible shift from this surface scattering effect, assuming that the K_B for this point is shifted down by 10 nW/K by the addition of the film. This maximum estimation, which likely overestimates the surface scattering effects, does not bring the measured L back to L_0, and indeed still indicates a strong drop in $L(T)/L_0$ with decreasing T. The gray shaded region provides an estimate of the maximum uncertainty added by the surface scattering effects. This clarifies that Au_1 indeed shows a strongly T-dependent $L(T)$ that is in surprisingly good agreement with the theoretical curve with no impurity scattering. This is essentially the same observation made by Kojda *et al.* for highly crystalline, thin Ag nanowires [28]. It is even more unexpected here, however, considering the highly polycrystalline nature of our sample. Also note that though $L(T)$ matches a bulklike theoretical behavior, as shown in Figs. 5(a) and 5(c), both σ and k are strongly reduced from bulk values. The charge transport also shows very typical effects of impurity or grain-boundary scattering of electrons. The agreement of $L(T)$ with the theory here indicates that e-ph scattering remains important, such that the balance of WF "obeying" horizontal scattering events and WF violating vertical scattering events evolves with T as expected in bulk systems. As films grow thicker, this balance tips strongly toward the violating vertical e-ph scattering events.

Figure 7 explores estimates of the relevant length and characteristic time of these scattering events. We first examine the estimated electron mean free path including all scattering events affecting thermal processes, $\ell_{k,tot}$, determined from the measured k using the kinetic expression $k = 1/3 c_{el} v_F \ell_{k,tot}$ with $c_{el} = \gamma T$ the electronic specific heat and v_F the Fermi velocity, using typical values [48]. The right-hand axis plots the relaxation time $\tau_{k,tot}$. We show calculations for three Au films, the $t = 19$ nm Au_1, the full sequential stack Au_{1-9} with $t = 372$ nm, and the single-shot film Au_0 with $t = 305$ nm. The gray area indicates the estimated in-plane grain size, $d_{g,IP}$, for the $t = 19$ nm thick Au_1 film, which is similar to the total average grain size for this thinnest Au film. This estimate of mean free path shows that scattering of electrons involved in thermal transport in the Au_1 film occurs on a length scale commensurate with the in-plane grain size. $\ell_{k,tot}$ for thicker films remains $< d_{g,IP}$.

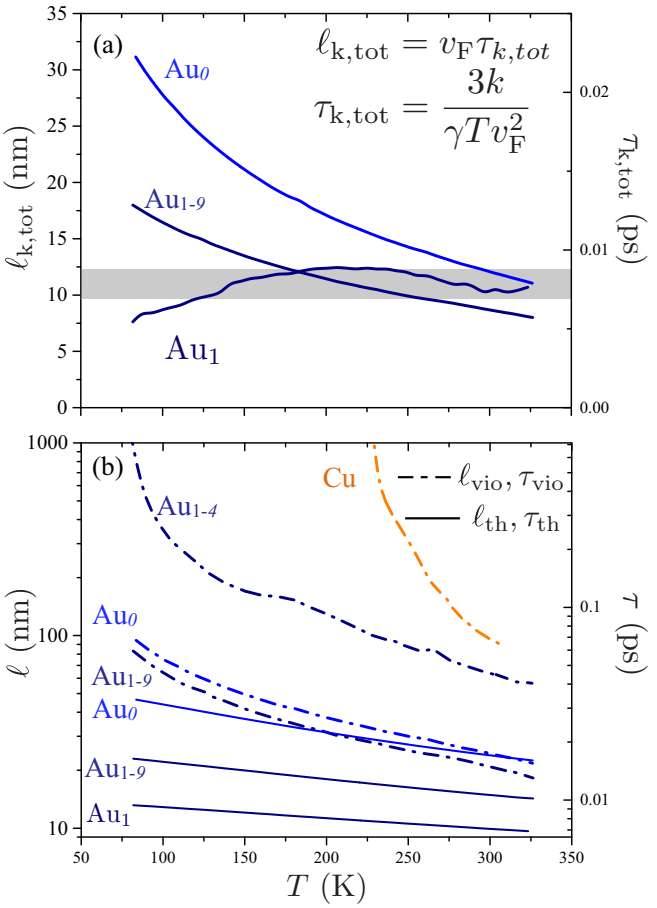

FIG. 7. (a) Estimated mean free path, $\ell_{k,tot}$ (left axis), and relaxation rate, $\tau_{k,tot}$ (right axis), for all electrons involved in thermal transport shown for three Au films. The gray band indicates the in-plane grain size for Au_1, centered at the estimated value 11 nm with width ±1.5 nm that most likely underestimates the uncertainty in $d_{g,IP}$. This is near $\ell_{k,tot}$ for all T for this film. Thicker films develop stronger T dependence, but have $\ell_{k,tot} < d_{g,IP}$ at all T ($d_{g,IP}$ from Table I, not shown here for Au_0 and Au_{1-9}). (b) Comparison of WF obeying and WF violating scattering events via ℓ (τ). ℓ_{th} (left axis) and τth (right axis) are shown for the same films as (a). ℓ_{vio} and τ_{vio} are shown for the same films though with Au_{1-4} shown rather than Au_1, which diverges due to much closer match with theory.

Using the theory of Eq. (6), we can make separate estimates of the length scale of scattering events that obey the WF theory and those that violate it. With the assumption that

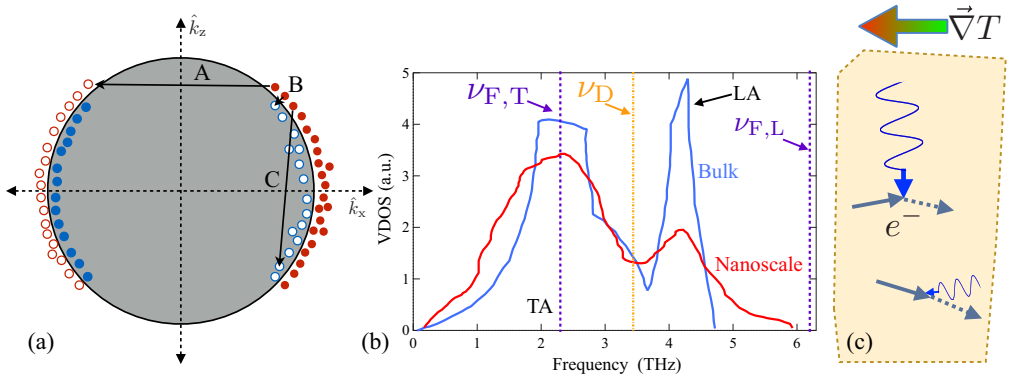

FIG. 8. (a) Schematic view of the Fermi sphere with a thermal gradient applied in the $\hat{x}$ direction. A, B, and C indicate three relevant electron-phonon scattering processes. As described in the main text, process A maintains the WF law, while both B and C lead to reductions of k without strongly affecting σ. (b) Schematic comparison of the VDOS for bulk (blue line) [49] and nanoscale Au (red line, adapted from Ref. [50]). The modification of VDOS, coupled with the anisotropy in grain size in the in-plane and out-of-plane directions, is a possible route to reduced k and violation of the WF law. The frequency scales of TA phonons and LA phonons corresponding to the Fermi momentum $\nu_{F,T}$ and $\nu_{F,L}$, respectively, as well as the frequency scale indicating the Debye temperature ν_D, are indicated. (c) A schematic view of a grain in one of our thicker Au films that shows the direction of the applied thermal gradient, and clarifies that larger q phonons allowed in the out-of-plane $\hat{z}$ direction cause scattering events that are preferentially of the C type, reducing in-plane k without strong effects on in-plane ρ.

Matthiessen's rule holds for the scattering time for thermal relaxation we write

$$\tau_{k,tot} = \left(\frac{1}{\tau_{th}} + \frac{1}{\tau_{vio}}\right)^{-1}. \quad (7)$$

Here τ_{th} is the scattering time including e-ph and impurity scattering underpinning Eq. (5) and τ_{vio} is the scattering time for the additional inelastic scattering that drives the WF violation. Using the typical derivation of the WF law, but replacing the simple ratio of scattering times for electrons in electrical transport, τ_σ, and those in thermal transport, $\tau_{k,tot}$, gives $L(T)/L_0 = \tau_{k,tot}/\tau_\sigma$, as we described elsewhere [16]. When deviations from L_0 are only from the processes considered in the theory of Eq. (6), then $L_{Th}(T)/L_0 = \tau_{th}/\tau_\sigma$, such that

$$\tau_{k,tot} = \left(\frac{L_0}{L_{Th}(T)\tau_\sigma} + \frac{1}{\tau_{vio}}\right)^{-1}. \quad (8)$$

Here $\tau_\sigma = m^*/\rho n e^2$ is calculated for Au using measured ρ and accepted electron density. Solving Eq. (8) allows calculation of τ_{vio} and comparison to the WF obeying scattering time τ_{th}.

Figure 7(b) shows the resulting calculation for τ_{th} and τ_{vio} (right axis) vs T for three films, with the mean free paths $\ell_{th} = \tau_{th} v_F$ and $\ell_{vio} = \tau_{vio} v_F$ (left axis) also shown. Note that we calculate τ_{vio} and ℓ_{vio} for Au_{1-4} instead of Au_1, since the latter largely obeys the $L(T)$ theory as shown in Fig. 6, such that ℓ_{vio} diverges. Here τ_{th} for each film takes into account the level of impurity scattering appropriate for that film, and this causes these WF obeying events to be dominated by the elastic, horizontal impurity scattering. These WF following scattering events occur at shorter ℓ and shorter τ than the WF violating scattering events. This indicates that electrons on average experience many WF obeying scattering events before a violating scattering event occurs. Note that long ℓ_{vio} and τ_{vio} indicate infrequent violating events, as is not uncommon for metals and as we previously reported for Cu (shown) and Al thin films [16]. The thicker Au films experience much more frequent WF violating scattering events, with Au_0 showing $\ell_{th} \approx \ell_{vio}$ near 300 K, indicating that the violating and traditional scatterings occur with roughly equal probability. However, separate examination of these violating scattering events does not indicate any particularly strong correlation with grain size.

A physical picture of the reduced in-plane k and WF violations in these Au films with nanoscale, columnar grains must explain the dominance of e-ph scattering for thin films, and the increasingly frequent WF violating scattering when t grows. We overview one possible explanation in Fig. 8. In panel (a), we clarify the nature of the e-ph scattering events relevant to the WF violation in these films. Following Ref. [1], we represent the Fermi sphere when a thermal gradient is applied in the in-plane ($\hat{x}$) direction. Both edges of the sphere are smeared, with empty and filled electron states that have higher than average thermal energy and lower than average thermal energy. Here hotter (cooler) states are shown with red (blue) circles, and filled (open) states are shown as filled (open) circles. We highlight three relevant scattering processes. Process A represents a "horizontal" scattering, where a hotter than average electron in a state with positive $\vec{k}_x$ is scattered by a phonon transferring sufficient momentum to place the electron in a state with nearly equal and opposite momentum. This reversal of direction can therefore affect both charge and heat transport, maintaining the assumption of equal scattering rates that yields the WF law. This normal scattering process (and its umklapp counterpart) requires a phonon with momentum $q \sim k_F$, and the reduction in population of these phonons drives the drop in $L(T)$ common in bulk materials and accounted for in the theory of Eq. (5). Process B represents a typical "vertical" scattering event, where a hot electron again in a state with positive $\vec{k}_x$ is scattered by a smaller q phonon into a cooler state but with nearly equal $\vec{k}_x$, affecting heat transport

with minimal effect on σ and thus violating the WF law. Process C represents scattering of a hot electron into a cold empty state by a larger q phonon but with momentum transfer predominantly in the out-of-plane $\hat{z}$ direction. This is again a WF violating vertical event.

We suggest that the change in the balance of these scattering events is driven by the evolution of the anisotropic nanoscale grains in these evaporated films, and ultimately by modification of the phonon, or vibrational density of states (VDOS) in nanoscale systems. VDOS for bulk systems is well understood theoretically and can be measured accurately for large, highly pure samples using inelastic neutron scattering (INS) [49]. The nature of this distribution of phonons with various energy has been explored more recently for either nanoparticle or nanostructured systems with particle or grain size ranging from 5 nm or less to as large as 120 nm. Such work started with theoretical predictions [51] that have been followed by molecular dynamics simulations [52] and a range of quite challenging experimental probes including Raman spectroscopy of Au nanoparticles [50,53] and INS of various nanocrystalline or nanostructured systems [54–57]. We represent the resulting picture from most of these studies schematically in Fig. 8(b). The bulk VDOS for Au measured by INS is shown for reference (blue line), and the peak at high frequency dominated by longitudinal acoustic (LA) modes is labeled. Transverse acoustic (TA) modes dominate the VDOS outside of this peak, though both types of modes can be found up to the maximum cutoff near 4.8 THz [49]. A nanoscaled system introduces undercoordinated and more loosely bound atoms at the boundaries of a grain or particle, which drives a somewhat counterintuitive redistribution of vibrational energies. We show this change schematically (in red, minimally smoothed data from a measurement for Au nanoparticles [50]). Here some TA phonon modes shift to lower energy while the typical longitudinal acoustic modes are broadened, with the effect of shifting many such modes to much higher energies. To clarify the effect of such shifts on e-ph scattering and the WF law we show the frequency of TA and LA phonons that carry momentum equal to the Fermi wave vector, $\nu_{F,T}$ and $\nu_{F,L}$, respectively (purple lines). We also show the scale of the average phonon vibrations represented by the Debye temperature for gold with $\nu_D = k_B\theta_D/h$ (orange line). Since a phonon of $q \sim k_F$ is needed for a horizontal scattering event such as process A, we see that reduction of the TA phonon peak near 2 THz will most like reduce horizontal scattering and potentially increase vertical scattering. However, the broadening of the LA phonon peak, with modes that are $\ll k_F$ in bulk such that they can only cause vertical scattering, most likely reduces the number of these events, while the LA modes that now approach $\nu_{F,L}$ could cause increased scattering of type A. Though the details will depend on the nature and size of the nanoscale grains, and recent work on Au nanowires has invoked modified VDOS as an explanation for reduced L [32], it is possible that the balance of type-A and type-B scattering events is not strongly altered by the nanoscale VDOS shifts alone, as we have observed for the Au_1 film. Furthermore, It is possible that the overall lowering of TA mode frequency could increase the e-ph coupling and cause more scattering events, such that these e-ph scattering events dominate impurity scattering as discussed above for Au_1.

However, if VDOS changes alone do not suppress $L(T)$, some other mechanism must be responsible for the strong reductions seen in the thicker films. Here we suggest that the growth of the grains in the out-of-plane direction introduces anisotropy in the phonon spectrum, such that phonons with momentum in the $\hat{z}$ direction recover a VDOS approaching bulk. This adds TA phonons with sufficient q to scatter across the Fermi sphere, allowing the type-C processes shown in Fig. 8(a), which relax the in-plane heat transport while not affecting charge transport, as shown schematically in Fig. 8(c). This matches the trends seen across this series of Au films. The nonequiaxed nature of the grains also suggests why thermal conductivity measurements such as time domain thermoreflectance [43,58,59], which typically measure k in the out-of-plane direction, might not observe the strong reduction of k in Au thin films that we have demonstrated.

Though this suggested mechanism matches our observations, there are certainly other possibilities that could be explored in a more detailed model or theory of this system. For example, the strong texturing of the nanoscale grains in our films could play a role, as the bulk VDOS of Au shows that the TA phonons are much lower energy (and momentum) for the (111) direction than for the (100) direction. Hence the small grain size in the in-plane (100) direction could preferentially cut off the higher-frequency phonons needed for horizontal scattering. However, an explanation for the overall thickness dependence of $L(T)$ is not clear in this picture.

Finally, we point out that this reduction of in-plane k could be general for materials with this pattern of grains and modification of VDOS. A broader exploration of such systems, focusing on semiconductors with large thermopower and potentially useful thermoelectric effects, could suggest a route to increasing the thermoelectric figure of merit in thin-film thermoelectric systems.

V. CONCLUSION

In summary, we presented measurements of in-plane charge and heat transport in well characterized, thermally evaporated Au thin-film samples. These measurements were made using a micromachined Si-N thermal isolation platform that isolates the in-plane transport properties and also allows examination of the Lorenz number and violation of the Wiedemann-Franz law with no uncertainty from sample geometry, since charge and heat transport are measured on exactly the same sample. These polycrystalline films, with in-plane grain size ranging between 10 and ≈50 nm and out-of-plane grain size roughly equal to film thickness, show dramatically reduced L compared to the free-electron value and values for other evaporated metal films. We suggest that this reduction results from anisotropic modification of the vibrational density of states of the system. Such a mechanism deserves further study and, if found to be more general, could suggest a route to increased performance of thermoelectric materials in thin-film form.

ACKNOWLEDGMENTS

We thank D. Bassett and A. D. Avery for helpful discussions and assistance in the laboratory, we thank J. Nogan and the IL staff at Center for Integrated Nanotechnologies (CINT) for guidance and training in fabrication techniques, and we gratefully acknowledge support from the National Science Foundation (NSF) (Grants No. DMR-1410247 and No. DMR-1709646). B.L.Z. also thanks the University of Minnesota Chemical Engineering and Materials Science Department, as a portion of this work benefited from support of the George T. Piercy Distinguished Visiting Professorship. Work at the University of Minnesota was supported primarily by NSF under Grant No. DMR-1807124. Parts of this work were carried out in the Characterization Facility, University of Minnesota, which receives partial support from NSF through the Materials Research Science and Engineering Center (MRSEC) program. This work was performed, in part, at the Center for Integrated Nanotechnologies, an Office of Science User Facility operated for the U.S. Department of Energy Office of Science by Los Alamos National Laboratory (Contract No. DE-AC52-06NA25396) and Sandia National Laboratories (Contract No. DE-AC04-94AL85000).

[1] J. M. Ziman, *Electrons and Phonons: The Theory of Transport Phenomena in Solids* (Clarendon, Oxford, 1960).

[2] G. S. Kumar, G. Prasad, and R. O. Pohl, Experimental determinations of the Lorenz number, J. Mater. Sci. **28**, 4261 (1993).

[3] H. Pfau, S. Hartmann, U. Stockert, P. Sun, S. Lausberg, M. Brando, S. Friedemann, C. Krellner, C. Geibel, S. Wirth, S. Kirchner, E. Abrahams, Q. Si, and F. Steglich, Thermal and electrical transport across a magnetic quantum critical point, Nature (London) **484**, 493 (2012).

[4] M. A. Tanatar, J. Paglione, C. Petrovic, and L. Taillefer, Anisotropic violation of the Wiedemann-Franz law at a quantum critical point, Science **316**, 1320 (2007).

[5] N. Wakeham, A. F. Bangura, X. Xu, J.-F. Mercure, M. Greenblatt, and N. E. Hussey, Gross violation of the Wiedemann–Franz law in a quasi-one-dimensional conductor, Nat. Commun. **2**, 396 (2011).

[6] M. G. Vavilov and A. D. Stone, Failure of the Wiedemann-Franz law in mesoscopic conductors, Phys. Rev. B **72**, 205107 (2005).

[7] M.-R. Li and E. Orignac, Heat conduction and Wiedemann-Franz law in disordered Luttinger liquids, Europhys. Lett. **60**, 432 (2002).

[8] C. L. Kane and M. P. A. Fisher, Thermal Transport in a Luttinger Liquid, Phys. Rev. Lett. **76**, 3192 (1996).

[9] A. C. Durst and P. A. Lee, Impurity-induced quasiparticle transport and universal-limit Wiedemann-Franz violation in d-wave superconductors, Phys. Rev. B **62**, 1270 (2000).

[10] B. Kubala, J. König, and J. Pekola, Violation of the Wiedemann-Franz Law in a Single-Electron Transistor, Phys. Rev. Lett. **100**, 066801 (2008).

[11] S. Lee, K. Hippalgaonkar, F. Yang, J. Hong, C. Ko, J. Suh, K. Liu, K. Wang, J. J. Urban, X. Zhang, C. Dames, S. A. Hartnoll, O. Delaire, and J. Wu, Anomalously low electronic thermal conductivity in metallic vanadium dioxide, Science **355**, 371 (2017).

[12] N. Mosso, U. Drechsler, F. Menges, P. Nirmalraj, S. Karg, H. Riel, and B. Gotsmann, Heat transport through atomic contacts, Nat. Nanotechnol. **12**, 430 (2017).

[13] L. Cui, W. Jeong, S. Hur, M. Matt, J. C. Klöckner, F. Pauly, P. Nielaba, J. C. Cuevas, E. Meyhofer, and P. Reddy, Quantized thermal transport in single-atom junctions, Science **355**, 1192 (2017).

[14] R. Sultan, A. D. Avery, J. M. Underwood, S. J. Mason, D. Bassett, and B. L. Zink, Heat transport by long mean free path vibrations in amorphous silicon nitride near room temperature, Phys. Rev. B **87**, 214305 (2013).

[15] B. L. Zink, B. Revaz, J. J. Cherry, and F. Hellman, Measurement of thermal conductivity of thin film samples using micromachined Si-N membrane calorimeters, Rev. Sci. Instrum. **76**, 024901 (2005).

[16] A. D. Avery, S. J. Mason, D. Bassett, D. Wesenberg, and B. L. Zink, Thermal and electrical conductivity of approximately 100-nm permalloy, Ni, Co, Al, and Cu films and examination of the Wiedemann-Franz law, Phys. Rev. B **92**, 214410 (2015).

[17] B. L. Zink, A. D. Avery, R. Sultan, D. Bassett, and M. R. Pufall, Exploring thermoelectric effects and Wiedemann-Franz violation in magnetic nanostructures via micromachined thermal platforms, Solid State Commun. **150**, 514 (2010).

[18] R. Sultan, A. D. Avery, G. Stiehl, and B. L. Zink, Thermal conductivity of micromachined low-stress silicon-nitride beams from 77 − 325 K, J. Appl. Phys. **105**, 043501 (2009).

[19] A. Jain and A. J. H. McGaughey, Thermal transport by phonons and electrons in aluminum, silver, and gold from first principles, Phys. Rev. B **93**, 081206(R) (2016).

[20] Y. Wang, Z. Lu, and X. Ruan, First principles calculation of lattice thermal conductivity of metals considering phonon-phonon and phonon-electron scattering, J. Appl. Phys. **119**, 225109 (2016).

[21] Z. Tong, S. Li, X. Ruan, and H. Bao, Comprehensive first-principles analysis of phonon thermal conductivity and electron-phonon coupling in different metals, Phys. Rev. B **100**, 144306 (2019).

[22] L. Lindsay, A. Katre, A. Cepellotti, and N. Mingo, Perspective on ab initio phonon thermal transport, J. Appl. Phys. **126**, 050902 (2019).

[23] H. Wang, J. Liu, X. Zhang, and K. Takahashi, Breakdown of Wiedemann-Franz law in individual suspended polycrystalline gold nanofilms down to 3 K, Int. J. Heat Mass Transf. **66**, 585 (2013).

[24] H.-D. Wang, J.-H. Liu, X. Zhang, Z.-Y. Guo, and K. Takahashi, Experimental study on the influences of grain boundary scattering on the charge and heat transport in gold and platinum nanofilms, Heat Mass Transf. **47**, 893 (2011).

[25] Q. G. Zhang, B. Y. Cao, X. Zhang, M. Fujii, and K. Takahashi, Influence of grain boundary scattering on the electrical and thermal conductivities of polycrystalline gold nanofilms, Phys. Rev. B **74**, 134109 (2006).

[26] R. Xia, J. L. Wang, R. Wang, X. Li, X. Zhang, X.-Q. Feng, and Y. Ding, Correlation of the thermal and electrical conductivities of nanoporous gold, Nanotechnology **21**, 085703 (2010).

[27] N. T. Eigenfeld, J. C. Gertsch, G. D. Skidmore, S. M. George, and V. M. Bright, Electrical and thermal conduction in ultra-thin freestanding atomic layer deposited W nanobridges, Nanoscale **7**, 17923 (2015).
[28] D. Kojda, R. Mitdank, M. Handwerg, A. Mogilatenko, M. Albrecht, Z. Wang, J. Ruhhammer, M. Kroener, P. Woias, and S. F. Fischer, Temperature-dependent thermoelectric properties of individual silver nanowires, Phys. Rev. B **91**, 024302 (2015).
[29] Z. Cheng, L. Liu, S. Xu, M. Lu, and X. Wang, Temperature dependence of electrical and thermal conduction in single silver nanowire, Sci. Rep. **5**, 10718 (2015).
[30] F. Volklein, H. Reith, T. W. Cornelius, M. Rauber, and R. Neumann, The experimental investigation of thermal conductivity and the Wiedemann-Franz law for single metallic nanowires, Nanotechnology **20**, 325706 (2009).
[31] J. Wang, H. Yu, T. Walbert, M. Antoni, C. Wang, W. Xi, F. Muench, J. Yang, Y. Chen, and W. Ensinger, Electrical and thermal conductivities of polycrystalline platinum nanowires, Nanotechnology **30**, 455706 (2019).
[32] S. D. Sawtelle and M. A. Reed, Temperature-dependent thermal conductivity and suppressed Lorenz number in ultrathin gold nanowires, Phys. Rev. B **99**, 054304 (2019).
[33] T. Starz, U. Schmidt, and F. Volklein, Microsensor for in-situ thermal-conductivity measurements of thin-films, Sensors And Materials **7**, 395 (1995).
[34] P. Nath and K. Chopra, Thermal conductivity of copper films, Thin Solid Films **20**, 53 (1974).
[35] T. M. Tritt, *Thermal Conductivity* (Kluwer, New York, 2004).
[36] T. Zhu, Y. Liu, C. Fu, J. P. Heremans, J. G. Snyder, and X. Zhao, Compromise and synergy in high-efficiency thermoelectric materials, Adv. Mater. **29**, 1605884 (2017).
[37] A. Zevalkink, D. M. Smiadak, J. L. Blackburn, A. J. Ferguson, M. L. Chabinyc, O. Delaire, J. Wang, K. Kovnir, J. Martin, L. T. Schelhas, T. D. Sparks, S. D. Kang, M. T. Dylla, G. J. Snyder, B. R. Ortiz, and E. S. Toberer, A practical field guide to thermoelectrics: Fundamentals, synthesis, and characterization, Appl. Phys. Rev. **5**, 021303 (2018).
[38] X. Zhou, Y. Yan, X. Lu, H. Zhu, X. Han, G. Chen, and Z. Ren, Routes for high-performance thermoelectric materials, Mater. Today **21**, 974 (2018).
[39] Y. Zhou, Y.-Q. Zhao, Z.-Y. Zeng, X.-R. Chen, and H.-Y. Geng, Anisotropic thermoelectric properties of Weyl semimetal NbX (X = P and As): A potential thermoelectric material, Phys. Chem. Chem. Phys. **21**, 15167 (2019).
[40] Y. Dubi and M. Di Ventra, Colloquium: Heat flow and thermoelectricity in atomic and molecular junctions, Rev. Mod. Phys. **83**, 131 (2011).
[41] Z.-G. Chen, G. Han, L. Yang, L. Cheng, and J. Zou, Nanostructured thermoelectric materials: Current research and future challenge, Prog. Nat. Sci.: Mater. Inter. **22**, 535 (2012).
[42] T. G. Novak, K. Kim, and S. Jeon, 2D and 3D nanostructuring strategies for thermoelectric materials, Nanoscale **11**, 19684 (2019).
[43] W. Wang and D. G. Cahill, Limits to Thermal Transport in Nanoscale Metal Bilayers Due to Weak Electron-Phonon Coupling in au and cu, Phys. Rev. Lett. **109**, 175503 (2012).
[44] C. V. Thompson, Structure evolution during processing of polycrystalline films, Annu. Rev. Mater. Sci. **30**, 159 (2000).
[45] C. Y. Ho, R. W. Powell, and P. E. Liley, Thermal conductivity of the elements: A comprehensive review, J. Phys. Chem. Ref. Data **3**, 1 (1974).
[46] R. A. Matula, Electrical resistivity of copper, gold, palladium, and silver, J. Phys. Chem. Ref. Data **8**, 1147 (1979).
[47] R. E. B. Makinson, The thermal conductivity of metals, Math. Proc Cambridge Philo. Soc. **34**, 474 (1938).
[48] C. Kittel, *Introduction to Solid State Physics*, 7th ed. (Wiley, New York, 1996).
[49] J. W. Lynn, H. G. Smith, and R. M. Nicklow, Lattice dynamics of gold, Phys. Rev. B **8**, 3493 (1973).
[50] M. Bayle, N. Combe, N. M. Sangeetha, G. Viau, and R. Carles, Vibrational and electronic excitations in gold nanocrystals, Nanoscale **6**, 9157 (2014).
[51] A. Kara and T. S. Rahman, Vibrational Properties of Metallic Nanocrystals, Phys. Rev. Lett. **81**, 1453 (1998).
[52] P. M. Derlet, R. Meyer, L. J. Lewis, U. Stuhr, and H. Van Swygenhoven, Low-Frequency Vibrational Properties of Nanocrystalline Materials, Phys. Rev. Lett. **87**, 205501 (2001).
[53] R. Carles, P. Benzo, B. Pécassou, and C. Bonafos, Vibrational density of states and thermodynamics at the nanoscale: The 3D-2D transition in gold nanostructures, Sci. Rep. **6**, 39164 (2016).
[54] B. Fultz, C. C. Ahn, E. E. Alp, W. Sturhahn, and T. S. Toellner, Phonons in Nanocrystalline ^{57}Fe, Phys. Rev. Lett. **79**, 937 (1997).
[55] H. Frase, B. Fultz, and J. L. Robertson, Phonons in nanocrystalline Ni_3 Fe, Phys. Rev. B **57**, 898 (1998).
[56] E. Bonetti, L. Pasquini, E. Sampaolesi, A. Deriu, and G. Cicognani, Vibrational density of states of nanocrystalline iron and nickel, J. Appl. Phys. **88**, 4571 (2000).
[57] R. Mazitov, V. Semenov, Y. Lebedev, R. Mulyukov, G. Raab, E. Yadrovskii, and V. Danilenko, Density of phonon states in nanostructured copper, JETP Lett. **92**, 238 (2010).
[58] D. G. Cahill, Analysis of heat flow in layered structures for time-domain thermoreflectance, Rev. Sci. Instrum. **75**, 5119 (2004).
[59] P. E. Hopkins, M. L. Bauer, J. C. Duda, J. L. Smoyer, T. S. English, P. M. Norris, T. E. Beechem, and D. A. Stewart, Ultrafast thermoelectric properties of gold under conditions of strong electron-phonon nonequilibrium, J. Appl. Phys. **108**, 104907 (2010).